Global Changes of the Water Cycle Intensity

MICHAEL G. BOSILOVICH, SIEGFRIED D. SCHUBERT, AND GREGORY K. WALKER

Global Modeling and Assimilation Office, NASA Goddard Space Flight Center, Greenbelt, Maryland

(Manuscript received 4 December 2003, in final form 16 June 2004)

ABSTRACT

In this study, numerical simulations of the twentieth-century climate are evaluated, focusing on the changes in the intensity of the global water cycle. A new model diagnostic of atmospheric water vapor cycling rate is developed and employed that relies on constituent tracers predicted at the model time step. This diagnostic is compared to a simplified traditional calculation of cycling rate, based on monthly averages of precipitation and total water content. The mean sensitivity of both diagnostics to variations in climate forcing is comparable. However, the new diagnostic produces systematically larger values with more variability.

Climate simulations were performed using SSTs of the early (1902–21) and late (1979–98) twentieth century along with the appropriate CO_2 forcing. In general, the increase of global precipitation with the increases in SST that occurred between the early and late twentieth century is small. However, an increase of atmospheric temperature leads to a systematic increase in total precipitable water. As a result, the residence time of water in the atmosphere increased, indicating a reduction of the global cycling rate. This result was explored further using a number of 50-yr climate simulations from different models forced with observed SST. The anomalies and trends in the cycling rate and hydrologic variables of different GCMs are remarkably similar. The global annual anomalies of precipitation show a significant upward trend related to the upward trend of surface temperature, during the latter half of the twentieth century. While this implies an increase in the simulated hydrologic cycle intensity, a concomitant increase of total precipitable water again leads to a decrease in the calculated global cycling rate. An analysis of the land/sea differences shows that the simulated precipitation over land has a decreasing trend, while the oceanic precipitation has an upward trend consistent with previous studies and the available observations. The decreasing continental trend in precipitation is located primarily over tropical land regions, with some other regions, such as North America, experiencing an increasing trend. Precipitation trends are diagnosed further using the water tracers to delineate the precipitation that occurs because of continental evaporation, as opposed to oceanic evaporation. These model diagnostics show that over global land areas, the recycling of continental moisture is decreasing in time. However, the recycling changes are not spatially uniform so that some regions, most notably over the United States, experience continental recycling of water that increases in time.

1. Introduction

The questions of how to define the water cycle intensity and whether it has changed can be addressed in several ways on both regional (Karl and Knight 1998; Chase et al. 2003; Bosilovich and Schubert 2001; Brubaker et al. 2001) and global scales. At the global scale, a simple method of estimating the global cycling rate or residence time uses long-term area averages of global precipitation and total water content (Chahine 1992; Trenberth 1998). For example, Chahine (1992) evaluated the global water cycle and storages and estimated the global atmospheric residence time (*e*-folding time) of water to be 10 days. This rate describes the turnover of the atmospheric storage of water and a time scale of global atmospheric water cycling. While this method is computationally efficient, the assumptions, which include neglecting moisture transport in the derivation, may be restrictive. Greenhouse gas experiments that use coupled ocean–atmosphere models indicate that, as temperature increases, the precipitation rate increases in response to increasing surface evaporation, and total precipitable water (TPW) increases with the

Corresponding author address: Dr. Michael G. Bosilovich, Global Modeling and Assimilation Office, Code 610.1, NASA Goddard Space Flight Center, Greenbelt, MD 20771.
E-mail: michael.bosilovich@nasa.gov

water-holding capacity of the atmosphere (e.g., Roads et al. 1996; Watterson 1998; Houghton et al. 2001). In AGCM experiments, Yang et al. (2003) show that the immediate effect of CO_2 warming in the atmosphere is to decrease the precipitation rate. Douville et al. (2002) found in numerical simulation that even with increased evaporation, TPW, and precipitation, the global cycling rate decreased. Global warming simulations also indicate that some increased continental drying (Wetherald and Manabe 1999) and increased risk of flooding (Milly et al. 2002) can occur. Kumar et al. (2004) found that in AGCM simulations using the last 50 yr of observed SST forcing, tropical precipitation over oceans increases with increasing SST, while tropical precipitation over land decreases with increasing SST.

Koster et al. (1986) and Joussaume et al. (1986) used passive atmospheric tracers in AGCMs to quantify the regional sources of water for global precipitation. In the present study, we have adopted this method and configured it to estimate the global cycling of water. The result is a quantitative estimate of global water cycling rate (or the inverse, called residence time) for atmospheric numerical models. This procedure for computing cycling rate does not require as many simplifications as the simple traditional method in the derivation of the water budget such as the use of long-term (monthly or annual) averages and global averages. Here, we have designed a numerical experiment to test the impact on global cycling of water of twentieth-century changes in SST. We also use long (50 yr) simulations with observed time-varying SST forcing to further study the impact of changing SSTs on the climate and cycling of water.

2. Methodology

a. Global water cycling

A simple calculation for determining the global water cycling rate can be derived from the atmospheric water vapor budget. If the water vapor budget is vertically integrated and area averaged, the water vapor budget reduces to

$$\frac{\partial Q}{\partial t} = E - P. \tag{1}$$

To determine the rate at which water leaves atmospheric storage, it is assumed that no water enters the atmosphere from surface evaporation (E), following Trenberth (1998):

$$\frac{\partial Q}{\partial} = -P. \tag{2}$$

Here, Q is the total precipitable water content of the atmosphere (in mm), and P is the precipitation (in mm day^{-1}). In this way, we can define a time constant $\lambda = P/Q$ and substitute into (2), obtaining

$$\frac{\partial Q}{\partial t} = -\lambda Q. \tag{3}$$

Integrating (3) from an initial time (t_0) to a future time (t), assuming that λ does not vary in time, the evolution of the total column water can be described by

$$Q(t) = Q(t_0)e^{-\lambda t}. \tag{4}$$

Therefore, $1/\lambda$ is the e-folding time (or residence time) of water in the atmosphere. The calculation of λ typically uses long-term (monthly, yearly, or climate) and global average total precipitable water and precipitation. The traditional approach is to use monthly or annually global averaged precipitation and total precipitable water to determine λ, the cycling rate of water in the atmosphere (e.g., Trenberth 1998; Douville et al. 2002).

b. Model

The primary atmospheric numerical model used in this study is the Finite Volume General Circulation Model (FVGCM; Lin 2004). The finite volume dynamical core uses a terrain-following Lagrangian control volume vertical coordinate system (Lin and Rood 1999; Lin 2004; Collins et al. 2004). The FVGCM dynamical core formulation includes a conservative Flux-Form Semi-Lagrangian (FFSL) transport algorithm (Lin and Rood 1996) with Gibbs oscillation-free monotonicity constraint on subgrid distribution. The FFSL has consistent and conservative transport of air mass and absolute vorticity (Lin and Rood 1997). This feature of the system makes the FFSL particularly useful for water vapor and passive tracer simulations.

The physical parameterizations of the FVGCM are based on National Center for Atmospheric Research (NCAR) Community Climate Model version 3.0 (CCM3) physics. The NCAR CCM3 parameterizations are a collection of physical processes with a long history of development and documentation (Kiehl et al. 1998). The moist physics package includes the Zhang and McFarlane (1995) deep convective scheme, which handles updrafts and downdrafts and operates in conjunction with the Hack (1994) mid- and shallow convection scheme. For radiation, the longwave radiative transfer is based on an absorptivity–emissivity formulation (Ramanathan and Downey 1986), and the shortwave radiative parameterization uses the δ-Eddington method (Briegleb 1992). The boundary layer mixing/turbulence

parameterization utilizes the "nonlocal" formulation from Holtslag and Boville (1993). In addition, the NCAR physical parameterization package includes orographic gravity wave drag based on McFarlane (1987). The land surface parameterization is that of Bonan (1998). The basic climatology of this configuration of FVGCM with CCM3 physics is described in Chang et al. (2001). The validation of regional aspects of the simulated hydrological cycle are discussed by Bosilovich et al. (2003), and the surface energy budget is evaluated by Betts et al. (2003).

The model also includes water vapor tracers (WVTs) to quantify the geographical source of water for global precipitation (Bosilovich and Schubert 2002; Bosilovich 2002; Bosilovich et al. 2003). In the typical configuration, the source of water for a tracer is the evaporation from a prescribed region. In the present model configuration, when the tracer sources include the whole globe, the sum of all WVTs is identical to the model's atmospheric moisture prognostic variable (in three spatial dimensions and time). In addition to such diagnostics as the oceanic and continental sources of water, the WVTs can be used to numerically solve for (2). For example, a WVT can be defined initially as equal to the model's specific humidity. This humidity is then predicted as a passive tracer (separate and distinct from the model's specific humidity prognostic variable) without a source of surface evaporation but including tracer transport and precipitation and turbulent tendencies, using

$$\frac{\partial q_T}{\partial t} = -\nabla_3 \cdot (q_T V) + \frac{\partial q_T}{\partial t_{\text{turb}}} + \frac{\partial q_T}{\partial t_{\text{Prec}}}, \qquad (5)$$

where q_T is the three-dimensional water vapor tracer, V is the three-dimensional wind, turb denotes the turbulent tendency not including surface evaporation (vertically integrates to zero), and Prec denotes the sum of all tracer precipitation tendencies (including condensation, rain evaporation, and convective vertical movement; vertically integrates to $-P_T$). The tracer precipitation tendencies are computed proportional to the total precipitation tendency, where the proportionality is based on the ratio of tracer water to total water (Bosilovich and Schubert 2002).

In the present experiments, we initialize a WVT equal to specific humidity at the beginning of each season (the first day of December, March, June, and September) and do not permit evaporation to enter the WVT as a source [following (3)]. Without evaporation as a source, the water in this WVT moves around the globe while precipitating until there is little or no water left (after 45 days, the water is approximately two orders of magnitude smaller than the initial condition). Vertical integration and global averaging of the WVT [q_T in (5)] prognostic equation results in an expression

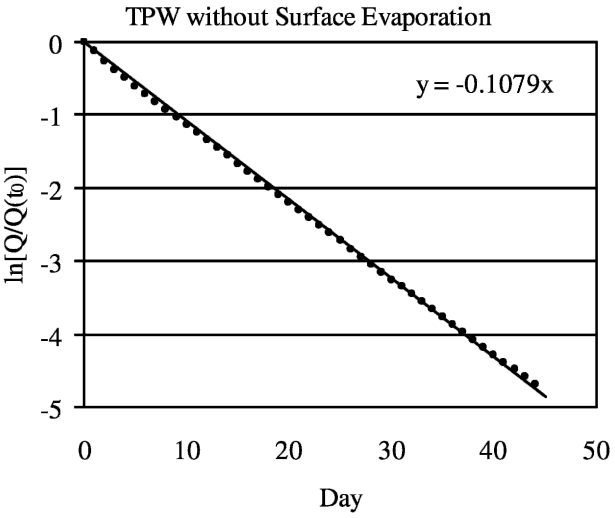

FIG. 1. Time series of a WVT (log of the tracer divided by its day-1, average value) initialized equal to the prognostic specific humidity. Precipitation and transport are permitted, and evaporation is not included in the tracer budget. The solid line indicates the linear regression of the data assuming zero intercept. The slope is the global cycling rate, and its inverse is the residence time of water in the atmosphere.

similar to (2). The difference between the two methods is that the tracer precipitation (P_T) acts to diminish tracer water at each model time step and grid point, whereas the long-term average of precipitation is used in the simple calculation. To determine λ for the WVT method, we rewrite (3) for the tracer and solve

$$\ln[Q_T(t)/Q_T(t_0)] = -\lambda t, \qquad (6)$$

assuming zero intercept [where $Q_T(t)$ is the daily global average of the vertically integrated tracer water content, and t_0 is the initial day]. Figure 1 shows daily averages of the vertically integrated global average WVT content for this calculation. On day 1, the WVT is nearly identical to specific humidity. The log of the daily WVT content follows a linear decrease as described by (6). The slope of the line estimates λ. In this example, the linear regression of the WVT data gives λ equal to 0.108 day^{-1} (or a residence time of 9.27 days). On the other hand, using the time average of the precipitation and total precipitable water (for the same period) yields a residence time of 7.55 days. For a given value of precipitation, the increase of TPW needed to increase the simple calculation of residence time by 2 days would be unrealistic. In addition, monthly variations of global TPW are on the order of 0.1 mm, so it is not likely that variations or even bias in the initial condition of the WVT leads to the larger values of residence time. Using monthly mean data to calculate λ

implies that the mean precipitation rate and water content exists throughout the period, but the WVT calculation allows the precipitation rate and water content to vary in time and space (and including transport), and the global averaging is performed as a post-processing step. In principal, the WVT method implements (2) into the GCM as a prognostic passive tracer. Water in heavily precipitating regions will dry first, while water in low precipitating regions must travel some time before being precipitated. This could lead to larger residence times than a simple time-averaged global ratio of TPW and precipitation.

c. Experimental design

The purpose of these experiments is to assess the impact of changes in the sea surface temperature (SST) and carbon dioxide concentration on the cycling of water and to study the usefulness of the WVT method for studies of the global cycling of water. The Hadley Centre SST data consist of global gridded SSTs for the early 1900s through the present (Rayner et al. 1996, 2003). We average the SSTs to generate mean annual cycles for the early (1902–21) and late (1979–98) twentieth century. We use these SSTs in 15-yr climate simulations (following a 2-yr spinup period). Early 1900s (1900–20) carbon dioxide concentration from ice core measurement is 299.5 ppm (Etheridge et al. 1998). A present-day value for carbon dioxide concentration is 355 ppm. We have run the following five AGCM experiments:

1) EXP1 late-century SST, 355 ppm CO_2.
2) EXP2 late-century SST, 299.5 ppm CO_2.
3) EXP3 early-century SST, 355 ppm CO_2.
4) EXP4 early-century SST, 299.5 ppm CO_2.
5) EXP5 late-century SST, 710 ppm CO_2.

For these simulations, the spatial resolution of the FVGCM is $2° \times 2.5°$. The simulations are designed to show the impact of SST and CO_2 on the simulated atmospheric climate. We focus on the cycling of global water vapor in atmosphere/land models (described in the next section). Note that, because we are running AGCM experiments, we do not include the affects of coupled oceanic–atmospheric feedbacks, nor do we consider other climate forcing such as those associated with land cover change, aerosols, and volcanoes.

We compute the global cycling of water in two ways. The water vapor tracer method is used as described in section 2b. At the beginning of each season (1 December, 1 March, 1 June, and 1 September), the WVT is reinitialized to the value of water vapor content at that time. The WVT is predicted forward in time, using proportional water vapor precipitation tendencies but not surface evaporation. In this way, we can estimate the global cycling rate of water [by (6)] once a season for 15 yr of each simulation by linear regression of tracer water for a 45-day period following initialization at the beginning of the season. After 45 days, the tracer water is so close to zero that the linearity does not hold well [in Fig. 1, $Q_T(t = 45 \text{ days}) = 0.2$ mm]. We also compute global cycling with the traditional method using the 45-day global averages of precipitation and total water in the systems (Chahine 1992; Trenberth 1998; Douville et al. 2002). Note that the 45-day averages may be referred to by seasonal names related to their initialization.

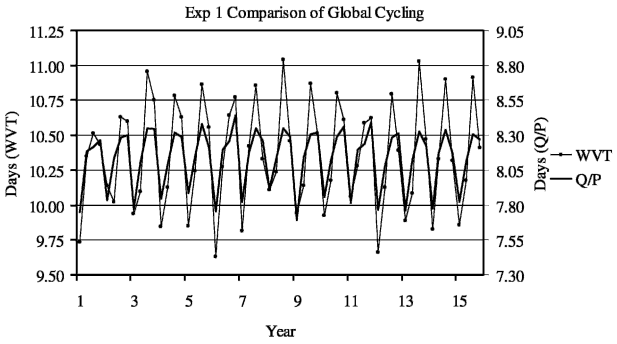

FIG. 2. Time series of seasonal residence time ($1/\lambda$) as diagnosed from the WVT method (scale on left axis) and the simple 45-day global average TPW and precipitation (scale on right axis) for 15 yr of EXP1 (using late-twentieth-century SST and CO_2).

3. Global cycling of water

a. Comparison of methods

Figure 2 shows the values of global cycling computed from the 45-day averages of total precipitable water and precipitation as well as the values computed from the WVT method for EXP1 (late-twentieth-century control). In the mean, the WVT method estimates a residence time that is 2.2 days longer than that based on the traditional calculation (note that each curve is associated with its own axis). The amplitude of the annual cycle of the residence time is larger for the WVT calculation, and greater interannual variability is apparent. This can be seen in the statistical analysis of the data (standard deviations and range of values; figure not shown). In another test, the averaging period for the simple calculation was shortened to the 15 days following WVT initialization. While the variability increased and the amplitude of the annual cycle slightly increased compared to the WVT method, subseasonal variability (not apparent in the WVT calculation) began to adversely affect the seasonal cycle.

A key difference is that the WVT method calculates new water contents at the model time step (and also in space), so that precipitation can only affect water

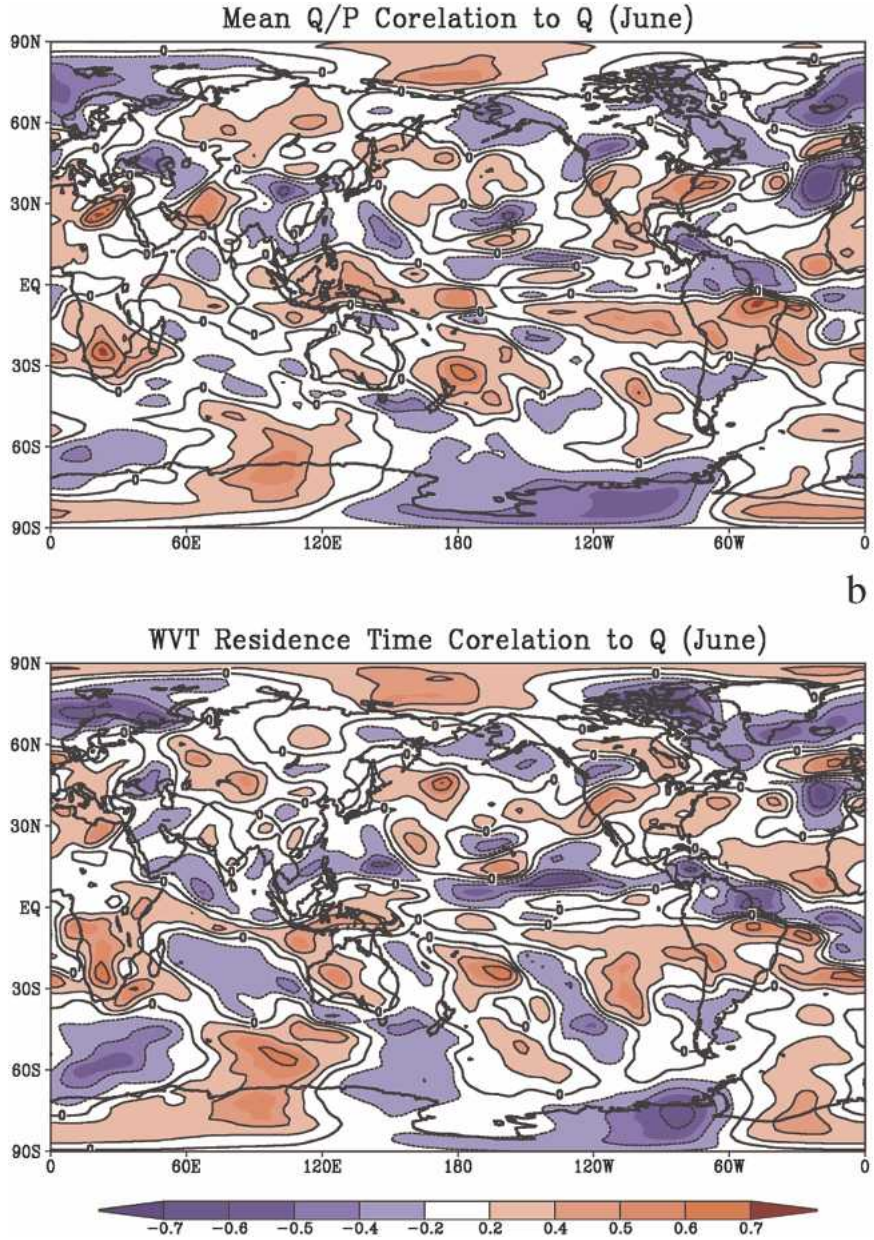

FIG. 3. Temporal correlation of the time series of Jun 45-day average residence time to the Jun TPW field for (a) mean *Q/P* method and (b) WVT residence time. Contours are present for the even shades.

vapor when there is remaining water vapor to be removed. Conversely, water vapor may remain in the simulated atmosphere longer in regions with little or no precipitation. Heavy regional precipitation, as in the Tropics, may cause water to drain quickly. However, once the regional water content is small, the heavy precipitation is less of a factor in the WVT cycling calculation. This is not accounted for in the traditional method using globally averaged TPW and precipitation. In this way, the water vapor tracer method produces values of residence time longer than the simple averages.

While there are differences in the mean values, there are substantial similarities between the two results. Figure 3 shows the temporal correlation of the different residence-time time series with the total precipitable water. The correlation patterns from both residence-time times series are generally similar at large scales.

TABLE 1. Correlation between WVT and simple method residence times for the 15 yr of the EXP1. "Annual cycle" is a correlation for all seasons in all years, and "annual means" is the correlation of the annual means of all 15 yr.

Period	Correlation
DJF	0.44
MAM	0.74
JJA	0.84
SON	0.73
Annual cycle	0.89
Annual means	0.64

Table 1 shows the correlation between the residence times computed from each method. While there is some seasonality in the correlation, namely, December–January–February (DJF, hereafter 3-month periods are denoted by the first letter of each respective month) correlation is smaller than the other seasons, the two calculations are reasonably well correlated. The smaller variability of the mean residence time calculation, noted in Fig. 2, seems to be more related to the application of global and time averaging in the calculation of the values.

b. Twentieth-century changes

In this part of the numerical experimentation, the goal is to discern the impact of global changes that have occurred over the twentieth century on the cycling of water and whether the more computationally expensive water vapor tracer calculation can provide additional information. Specifically, we examine the response of the climate system to changes in SSTs and carbon dioxide concentration (CO_2). Figure 4 shows the mean difference in the SST between the early and late twentieth century. While there are some negative anomalies in the Pacific Ocean and at high latitudes (due to sea ice variations), most of the global SST differences are positive. For example, the Indian Ocean and southern Atlantic Ocean are nearly 0.5 K warmer on average. The global mean is 0.37 K warmer in the late century compared to the early century (Fig. 5). While SSTs are warmer during all seasons in the late century, there is a seasonal cycle with June–July–August (JJA) having the largest seasonal increase. This seasonal cycle for global TPW, WVT residence time, and the simple method residence time (as well as the difference between residence times) follows a similar seasonal cycle.

Figure 6 shows the mean differences in precipitation and TPW between EXP1 and the other experiments. The combined effect of early- and late-century SST and CO_2 are shown in the differences between EXP1 and EXP4. The precipitation anomalies vary between regions, and most of the significant impact is over the ocean. The tropical precipitation patterns show positive and negative anomalies because of the shifting circulations, rather than a correlation to local SST differences (Fig. 4). However, the model indicates that precipita-

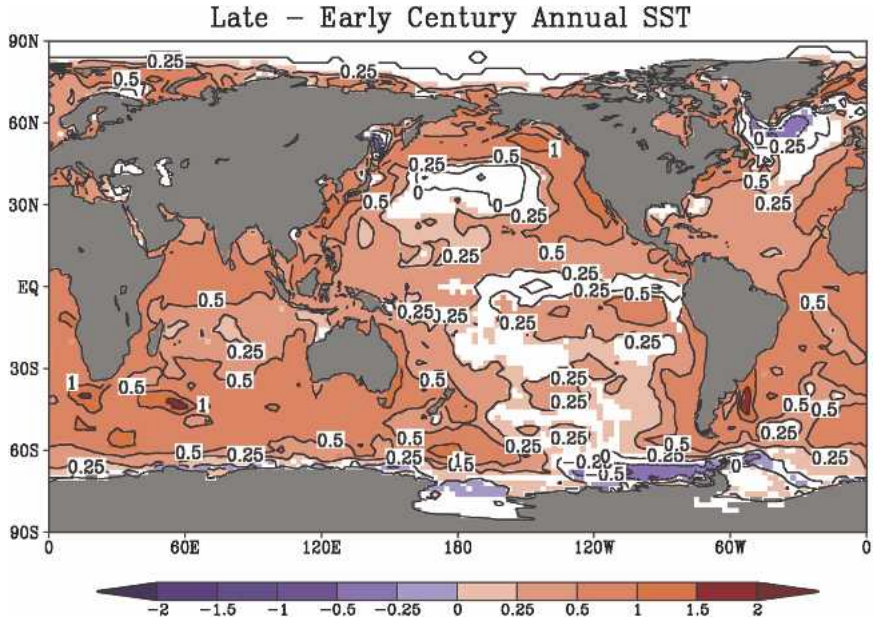

FIG. 4. Annual mean SST difference for the late century minus early century (contours at −0.5, –0.2, –0.1, 0, 0.1, 0.2, 0.5, 1.0, 1.5, 2.0 K). Color-shaded temperature differences are significant at the 5% level based on a *t* test.

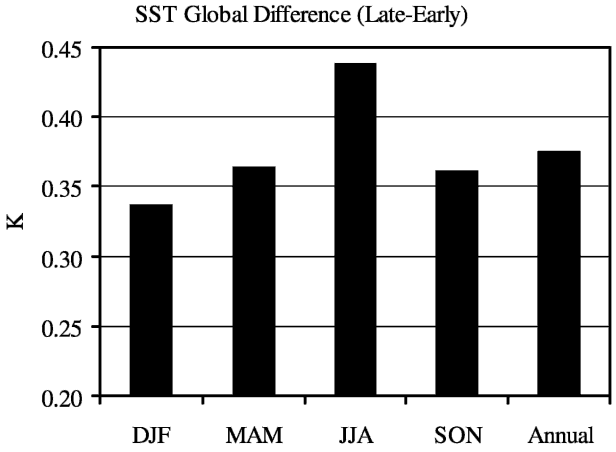

FIG. 5. Global average seasonal and annual difference of late-century minus early-century SST (Kelvin).

tion over the Amazon decreases for the late twentieth century, while the precipitation over the southwestern United States increases. This result is qualitatively similar to that found by Kumar et al. (2004) for the tropical precipitation over land. On the other hand, TPW increases almost everywhere, except where the SST differences are weak or negative (e.g., the central North Pacific and Tropics west of South America). The difference of EXP1 and EXP2 shows the direct impact of the change of CO_2 over the twentieth century, which is much less than the impact of the changes in SST alone (Fig. 6 b, c, f, g). Doubling the CO_2 (EXP5) increases the TPW and decreases the precipitation, compared to EXP1. However, the precipitation decrease is over ocean, where there is no feedback (i.e., surface temperature changes). The precipitation increases are over land, where there is feedback with the land surface parameterization, for example, in Africa and the Amazon. The net result is that the global precipitation decreases with increasing CO_2. A similar result was found by Yang et al. (2003), where increasing CO_2 (with prescribed SST) decreased the radiative cooling, which was balanced by a decrease in latent heating due to precipitation.

In a regional analysis, Chase et al. (2003) evaluated observations and the National Centers for Environmental Prediction (NCEP)–NCAR reanalysis to determine trends in large monsoon regions (Southeast Asia, eastern and western Africa, and Australia). All the cases studied showed decreasing trends in precipitation; however, the precipitation trends were not found to be significantly different from zero in Southeast Asia and western Africa. In the present simulation, there are few statistically significant differences in the monsoon regions (Fig. 6a). However, eastern Africa does have an increase of precipitation from the early to late twentieth century. In addition, the Mexican monsoon region experiences a local increase in precipitation.

Figure 7 shows the time and global average residence times computed from the WVT method and the simple method for each experiment. A mean difference of nearly 2.2 days is found between the methods for each experiment. In comparing the early-twentieth-century experiment (EXP4) and the late-century experiment (EXP1), the residence time of water in the atmosphere increases by approximately 0.2 days. Increasing the CO_2 and warming the SST both (thereby increasing evaporation and water-holding capacity of the atmosphere) act to increase the residence time. A doubling of the CO_2, while keeping the SST at the late-twentieth-century values, shows a 0.25-day increase in the residence time compared to the present-day control. These simulations show that an increase in SST or CO_2 can increase the TPW with less impact on precipitation (Table 2), thereby increasing the residence time of water in the atmosphere and slowing of the global water cycling rate. The similarity between the two cycling rate methods suggests that the basic response of the system to climate forcing can be reasonably investigated using the simple method. Of course, if the absolute magnitude or the interannual variability of residence time are required, the simple method data may be insufficient. In the next section, we evaluate the water cycling results further with real time-varying SSTs in several different global models.

4. 50-yr model integrations

a. FVGCM

To further investigate the cycling rate changes related to SST increases, a 50-yr model integration was performed with the FVGCM at $2° \times 2.5°$ horizontal resolution. Hadley Centre monthly varying SSTs provide the boundary forcing for the GCM for the period 1949–98, but the trend of CO_2 was not included (a present-day value was used). Figure 8 shows the time series of annual and global averaged surface temperature, precipitation, TPW, and residence time. The time series of temperature show slight cooling from the 1950s through mid-1970s and increasing temperatures from the 1970s through 1990s. Precipitation and TPW appear to correlate well with the surface temperature. The residence time (TPW/P) shows a mostly increasing trend (in contrast to the surface temperature time series) across the period. Surface evaporation is not shown, but its evolution is nearly identical to that of the precipitation (annually and globally averaged). Overall, the annual global means of precipitation, surface temperature, TPW, and residence time are all positively correlated (Table 3). In the next section, we will com-

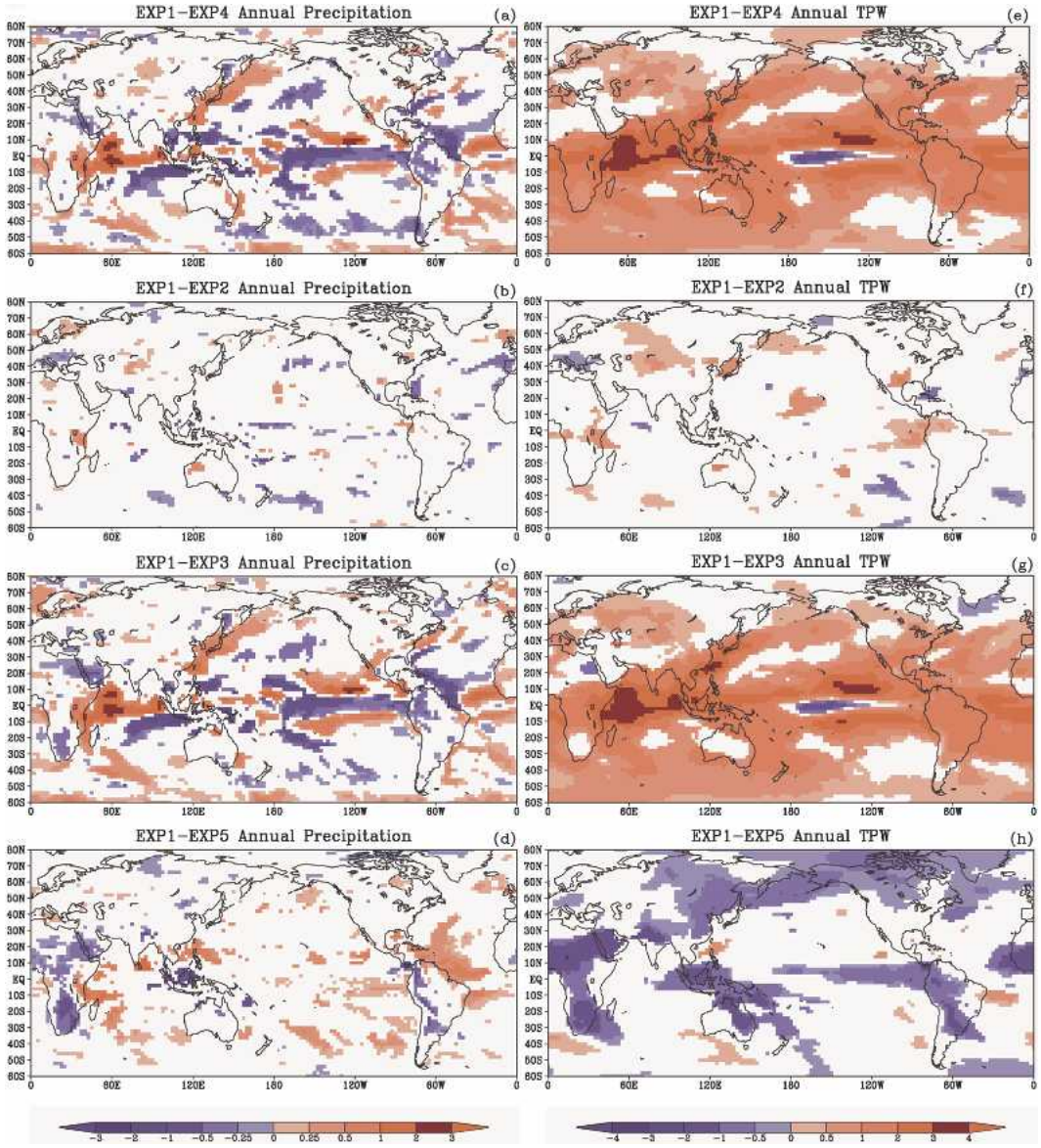

FIG. 6. Mean difference of EXP1 precipitation and TPW with each of the other experiments. Only values significant at the 5% level of the *t* test between each experiment are plotted.

pare the apparent FVGCM trend in the hydrologic cycle with those of other models.

b. Ensemble simulations

In participating in the Climate of the Twentieth Century Project (C20C), several GCM research groups are integrating their models for long periods of the twentieth century. In particular, ensemble simulations from the National Aeronautics and Space Administration's (NASA's) Seasonal to Interannual Prediction Project (NSIPP; 9 members) and the Center for Ocean, Land and Atmosphere (COLA; 10 members) are available for analysis. Here, we compare the ensemble means of these GCM integrations with the single FVGCM simulation discussed in the previous section. The COLA AGCM uses the dynamical core described by Kiehl et al. (1998) with semi-Lagrangian advection of moisture (Kinter et al. 1997; Dirmeyer and Zeng 1999; Schneider 2002). The land parameterization is the Simplified Biosphere Model (SSiB; Xue et al. 1991, 1996). The NSIPP (version 1) AGCM uses the dynamical core described by Suarez and Takacs (1995). The land param-

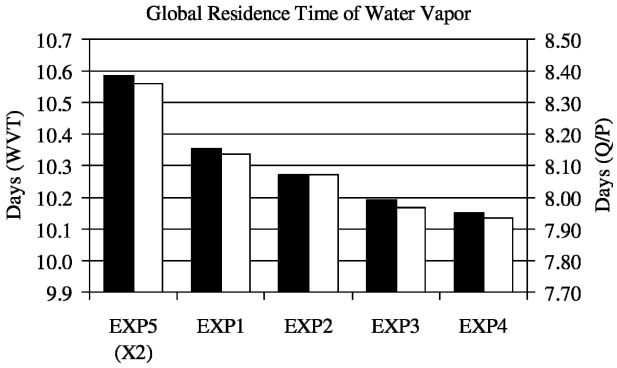

FIG. 7. The 15-yr average global mean residence time computed from WVTs (black bar, left axis) and the simple mean Q/P calculation (white bar, right axis).

eterization is the Mosaic land surface model (Koster and Suarez 1992). Both COLA and NSIPP AGCMs use the relaxed Arakawa–Schubert parameterization for deep convection (Moorthi and Suarez 1992). The NSIPP-1 model has been used in several predictability studies (Pegion et al. 2000; Schubert et al. 2002; Schubert et al. 2004). Straus et al. (2003) recently intercompared the NSIPP and COLA AGCMs in seasonal prediction experiments. The COLA model simulations are for the period 1949–97. All the other datasets are compared through 1998. The NSIPP and COLA simulations examined here are the initial contributions to the C20C project; in these experiments only the SST forcing is included (CO_2 is fixed at the present-day concentration).

TABLE 2. The 15-yr means of global precipitation (P) and TPW in each climate experiment.

15-yr avg	P (mm day^{-1})	TPW (mm)
EXP1	3.05	24.84
EXP2	3.07	24.78
EXP3	3.00	23.94
EXP4	3.02	23.93
EXP5	3.00	25.09

Each of the models has different mean states of the water cycle, so we focus on the anomalies from the 50-yr means. Figure 9 shows the globally averaged annual anomalies of surface temperature, precipitation, TPW, and residence time (TPW/P). In general, the GCM anomalies are all very well correlated, with increasing trends in precipitation, TPW, and residence time, especially since the mid-1970s. The values of the

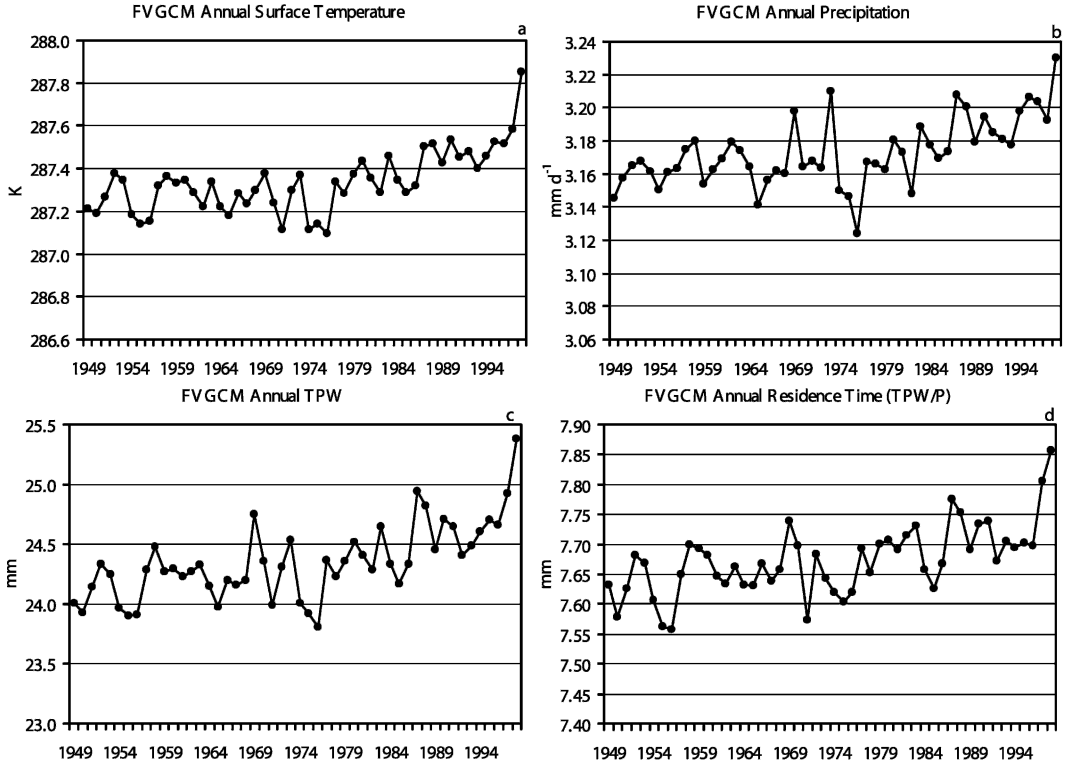

FIG. 8. FVGCM global and annual averaged (a) surface temperature, (b) precipitation, (c) total precipitable water, and (d) residence time (computed from the annual means of precipitations and TPW).

TABLE 3. Correlation between globally and annually averaged time series of precipitation (P), TPW, global residence time (TPW/P), and surface temperature (T_s). Correlations using detrended time series are in parentheses.

FVGCM	P	TPW	T_s
TPW	0.89 (0.83)		
T_s	0.84 (0.75)	0.95 (0.90)	
TPW/P	0.66 (0.47)	0.93 (0.88)	0.89 (0.81)

trends are presented in Table 4. The significance of the trends is tested by computing the t statistic for the trend line, and each trend is found to be significant at the 1% level (except where noted in the table).

At issue then is how the water cycle intensity is defined. In all the models, both precipitation and evaporation (not shown) are increasing, which may be interpreted as an intensification of the water cycle. On the other hand, the residence time is increasing, so the increasing trend of TPW is greater relative to the trend of precipitation. Therefore, the cycling rate of water (inverse of residence time) is decreasing, which may be interpreted as a lessening of the intensity of the water cycle. This result is similar to that found by Douville et al. (2002) using a coupled atmosphere–ocean GCM, and that of Roads et al. (1998) using the Community Climate Model version 3.

c. *Differences between continental and oceanic precipitation*

While the SSTs are driving the atmospheric changes, the role of the land surface is not clear. For example, with identical SSTs and different CO_2 levels, EXP1 and EXP5 show some differences that are likely related, in part, to the feedback with the land surface (Fig. 6h). Figure 10a shows the temporal correlation of the detrended annual time series residence time with the FVGCM annual surface temperature fields. An ENSO-like pattern is apparent in the Pacific Ocean extending into the Indian Ocean. However, the largest correlations are over the Caribbean Sea and extend across the tropical Atlantic Ocean. The maximum correlations

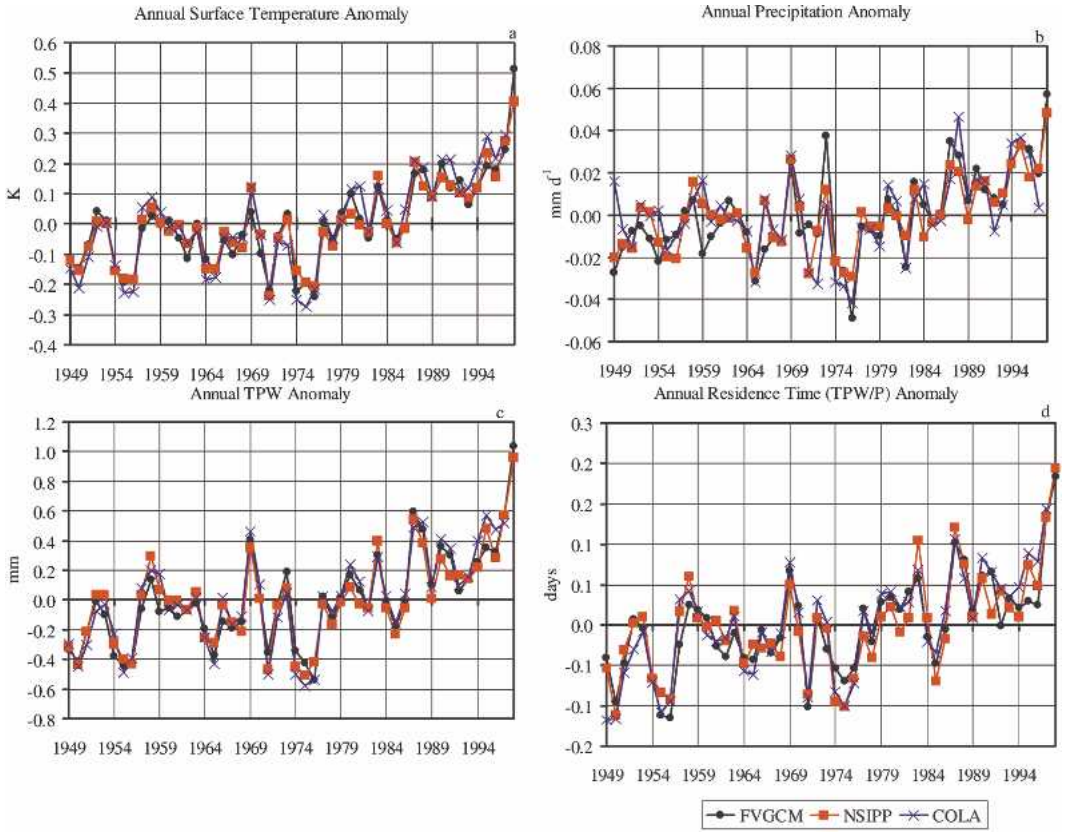

FIG. 9. Global and annual average anomalies from long-term means for (a) surface temperature, (b) precipitation, (c) total precipitable water, and (d) residence time. NSIPP and COLA GCM data are ensemble averages of 9 and 10 members, respectively.

TABLE 4. Trends of surface temperature, precipitation, TPW, and residence time (TPW/*P*) for the periods (a) 1949–98 and (b) 1974–98. The units of the variables are the amount of change per 50 yr. Using the *t* statistic, all trends are significant (the trend is significantly different from 0) at the 1% level, except the italicized values, which are significant at 5%. COLA data are evaluated through 1997.

(a) 1949–98

Trends (per 50 yr)	T_s (K)	P (mm day^{-1})	TPW (mm)	TPW/P (days)
FVGCM	0.32	0.04	0.71	0.13
NSIPP	0.30	0.03	0.60	0.12
COLA	0.34	*0.02*	0.64	0.14

(b) 1974–98

Trends (per 50 yr)	T_s (K)	P (mm day^{-1})	TPW (mm)	TPW/P (days)
FVGCM	0.90	0.13	1.78	0.26
NSIPP	0.85	0.10	1.83	0.34
COLA	0.93	0.11	1.85	0.31

also extend across the Amazon River basin. In addition, a substantial area of the Asian continent is positively correlated to the residence time. It seems reasonable that the residence time may be related to the evaporation through surface temperature. However, the correlation of global residence time with surface evaporation shows little resemblance to the correlation with surface temperature (Fig. 10b). For example, there is a negative correlation between the global residence time and Amazonian evaporation. The correlation of residence time with TPW more closely reflects the patterns of correlation with surface temperature (Fig. 10c), which may indicate that the relationship of residence time with SST may be more associated with the water-holding capacity of the atmosphere than the surface evaporation. In addition, Fu et al. (2001) show that seasonal warming of the SSTs in the east equatorial pacific contributes to subsidence and decreased precipitation over the eastern Amazon. We made similar comparisons with the NSIPP and COLA ensemble mean data, and the patterns are similar, but the correlations are stronger as would be expected for ensemble means (figures not shown).

We also averaged the precipitation over land and oceanic areas separately (Fig. 11). Contrary to the global average of precipitation, the land average of precipitation decreases across the 50-yr period. This agrees with the Global Historical Climatology Network (GHCN) land gauge observations (Vose et al. 1992), despite the irregularity of the observing network. Oceanic average of simulated precipitation increases in time. The magnitudes of the trends for land and oceanic averages are more than the global average (Table 5). The trends are quite similar for each model and the GHCN observations. In Fig. 12, the precipitation trend is computed at each grid point for the FVGCM, NSIPP, and COLA GCMs. There are remarkable regional similarities in the precipitation trends. Notable positive trends over the tropical Pacific Ocean, Indian Ocean, and Kurashio Current are apparent in each model. Notable negative trends over the Gulf of Mexico, Caribbean Sea, Amazon, central Africa, and north-central Pacific Ocean are likewise apparent in each model. The global decrease of continental precipitation is mostly related to the regional decreases of the tropical land areas (central Africa and Amazon). This agrees with the analysis of tropical precipitation in AGCM simulations by Kumar et al. (2004). The average decrease in precipitation over land is not uniform, as precipitation over the contiguous United States is generally increasing in all the GCMs. Also, the Fig. 11b time series of NSIPP oceanic precipitation has a larger trend than the other models. When considering all the oceanic grid points in Fig. 12, two-thirds of the NSIPP model grid points are positive, while only half of the FVGCM grid points exhibit a positive trend. This may indicate a difference in the way each model is tuned to SST in its convection and precipitation parameterizations. Figure 12d shows the trends of GHCN gauge precipitation gridded at 5° resolution. The large-scale trends in the central United States and Africa noted in the model simulation agree well with these observations.

In this FVGCM experiment, the WVTs were configured to represent geographical sources of water, as in Bosilovich and Schubert (2002) and Bosilovich et al. (2003). Specifically, WVTs were implemented to tag separately the surface evaporation from the continental and oceanic source regions. Initially, all tracer water was included in the ocean WVT, and land is zero; however, one year of data was rejected to allow for spinup of the WVTs. Figure 13a shows the time series of globally averaged FVGCM continental evaporation. The land evaporation is generally decreasing (see also Table 6). The precipitation over land from both land sources and oceanic sources is decreasing (Table 6 and Figs. 13b,c). Oceanic sources of precipitation over land appear to stabilize for the last 25 yr of the simulation (when surface temperatures are generally increasing). Continental sources of precipitation over land decrease over the 50-yr period. However, the decrease of land evaporation does not extend to the most recent 25 yr.

Figures 14a,b show the trend of precipitation from land sources and the trend of precipitation from oceanic sources. While these trends generally follow that of the total precipitation (Fig. 12a), several distinct differences are apparent. First, while trends in precipitation from oceanic sources are positive over the central United States, the values are relatively small and not statistically significant. However, the trend of precipitation from continental sources over the central United States is more significant. This differs from the tropical

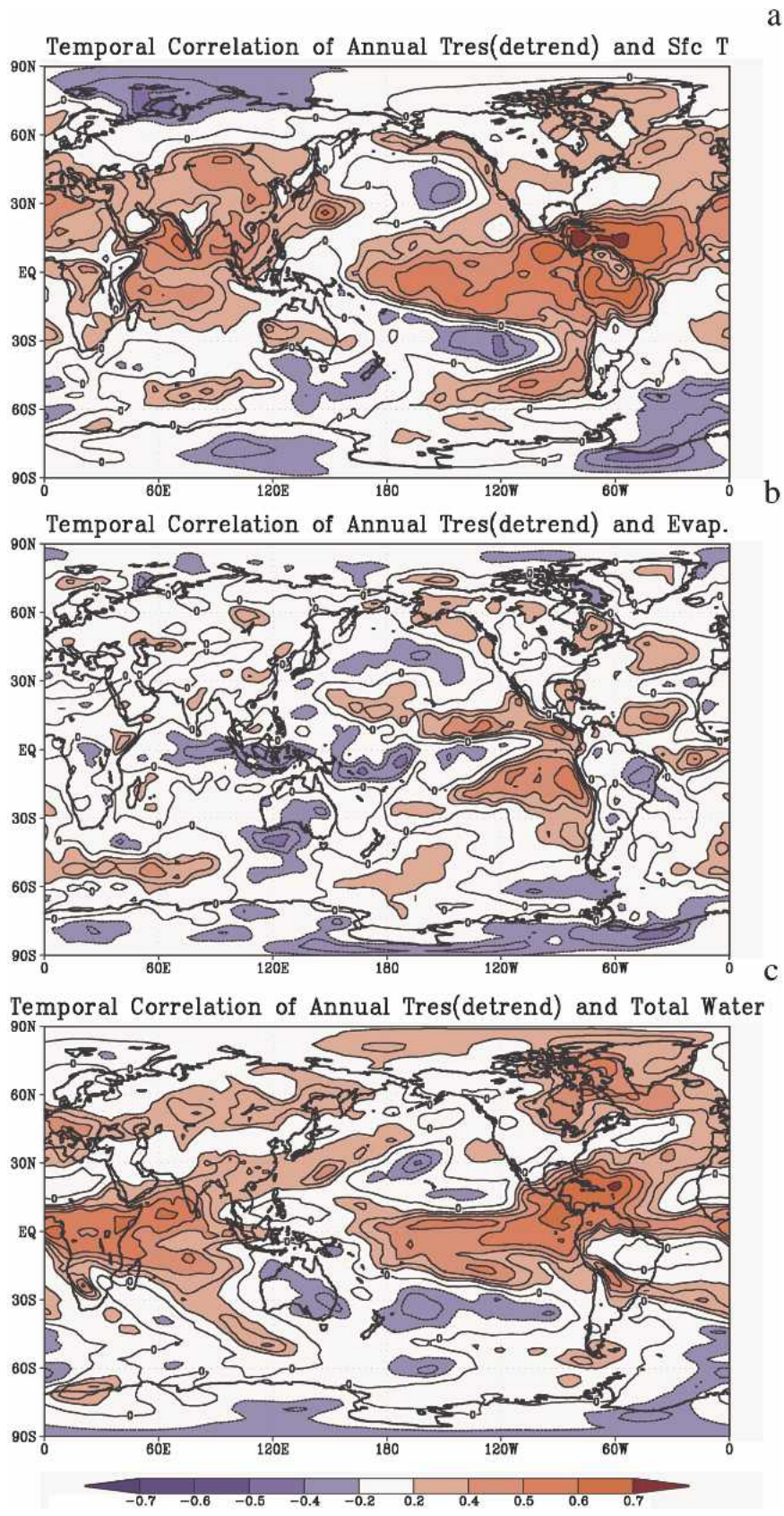
a
Temporal Correlation of Annual Tres(detrend) and Sfc T
b
Temporal Correlation of Annual Tres(detrend) and Evap.
c
Temporal Correlation of Annual Tres(detrend) and Total Water
90N
60N
30N
EQ
30S
60S
90S
0
60E
120E
180
120W
60W
−0.7 −0.6 −0.5 −0.4 −0.2 0.2 0.4 0.5 0.6 0.7

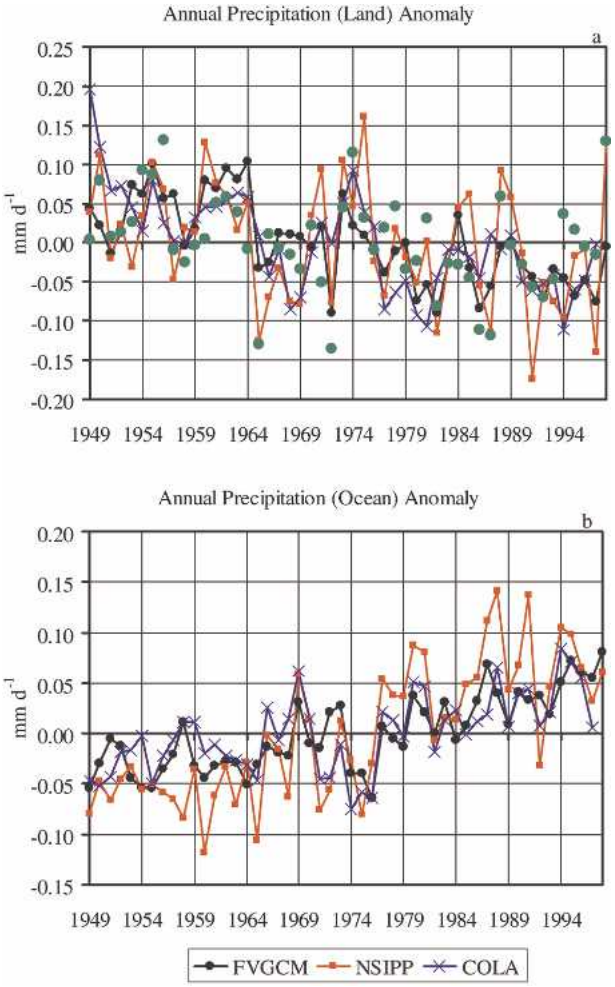

FIG. 11. Annual average anomalies from long-term means for (a) precipitation at global land grid points and (b) precipitation at global ocean grid points (including the Antarctic continent). The green dots are the global land-averaged GHCN gauge precipitation data.

land regions (specifically the Amazon and central Africa) where both trends in land and oceanic sources are large and comparable. The map of evaporation trend (Fig. 14c) is somewhat similar to the map of total precipitation trend (Fig. 12a; the spatial correlation of the significant values in these two figures is 0.62). Over land, the evaporation may be limited by precipitation, which can increase this correspondence.

TABLE 5. Trends as in Table 4a except for precipitation averages over land and oceanic regions only. Antarctica is considered in the oceanic average

Trend (per 50 yr)	*P* land (mm day^{-1})	*P* ocean (mm day^{-1})
FVGCM	−0.12	0.10
NSIPP	−0.08	0.17
COLA	−0.14	0.08
GHCN	*−0.06*	

Table 7 shows the trend of area-averaged precipitation, evaporation, and surface temperature for the Mississippi and Amazon River basins. The increasing trend of precipitation in the Mississippi basin is related to the increasing trend of precipitation from continental sources. This result agrees with Brubaker et al. (2001), who found that continental recycling of water, determined from observations and reanalysis data, is increasing in the Mississippi River basin. The evaporation within the Mississippi River basin is likewise increasing, but surface temperature changes do not experience a significant trend. In the Amazon, the precipitation trend is the result of changes in both continental and oceanic sources of water. The Amazon evaporation experiences little change over the whole period but experiences a more decreasing trend in the last half of the 50-yr period, while surface temperatures continually increase. While it is not the purpose of this paper to discuss the changes of regional water cycles in depth, this analysis demonstrates the range of regional variability of the water cycle intensity changes. Furthermore, the changes in continental precipitation and local cycling of water are likely seasonally dependent (as discussed by Wetherald and Manabe 1999).

5. Summary and conclusions

In this study, we estimate the global cycling rate of water in global atmospheric models using two methods. The traditional method can be applied to any model simulation but uses simplifying assumptions that may affect the result. The water vapor tracer (WVT) method for global cycling rate utilizes the capability of models' passive constituent tracers to predict a separate water vapor variable (parallel to specific humidity) that solves the water vapor budget without a source

←

FIG. 10. Map of the temporal correlation between the FVGCM detrended time series of annual residence time (Fig. 9 residence time, detrended) with annual FVGCM variables (a) surface temperature, (b) evaporation, and (c) total precipitable water. [(a) and (b) have been smoothed to highlight the large-scale features.]

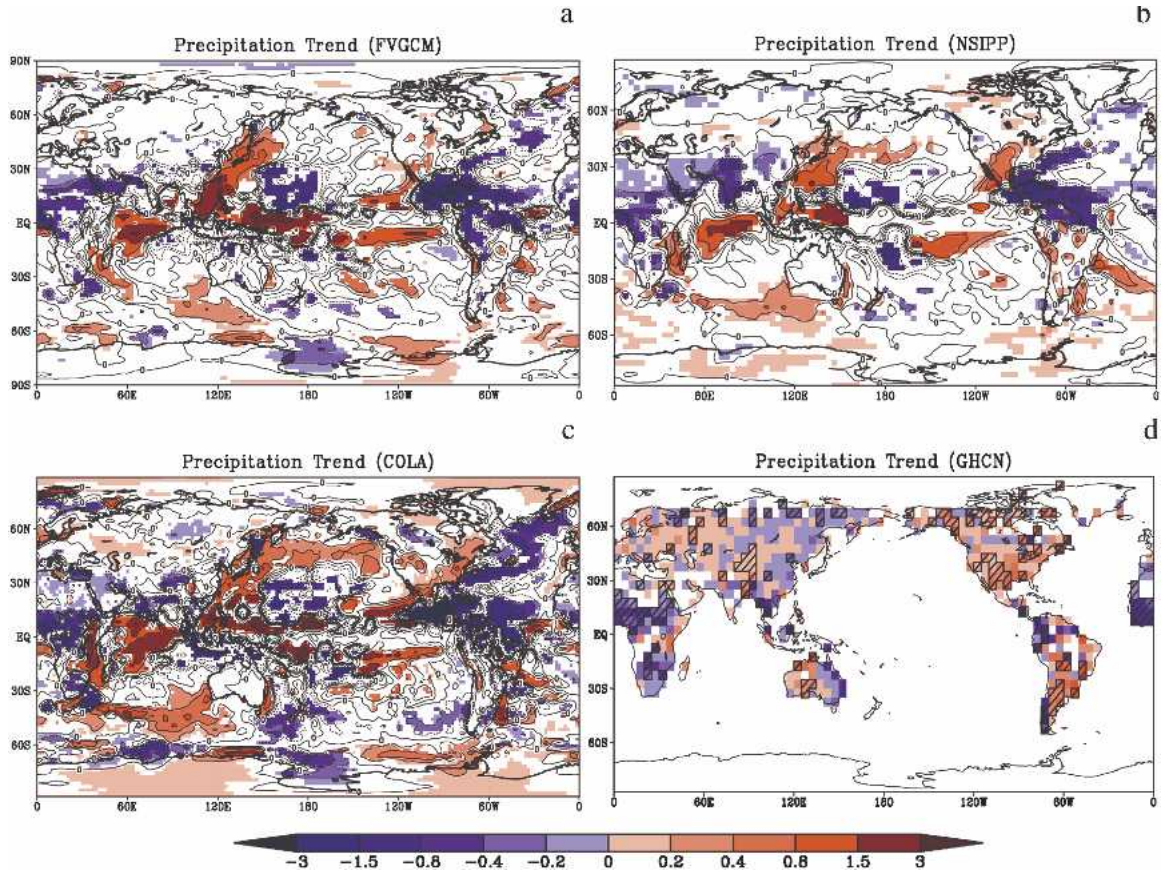

FIG. 12. Map of precipitation trends at model grid points for (a) FVGCM, (b) NSIPP, (c) COLA GCMs, and (d) GHCN gauge data. The units are mm day^{-1} (50 yr)$^{-1}$. For the GCMs, trends significant at the 5% level from *t* tests are color shaded, and all values are contoured in black. Crosshatched boxes denote the trends significant at the 5% level in the GHCN observations.

of surface water (evaporation). In contrast, the traditional cycling rate calculations simply use time-averaged precipitation and total precipitable water diagnostics and are more easily applied to models simulations or existing observations. While the WVT method did show greater interannual variability, different sensitivity to total water vapor, and higher mean values than the simpler method, the climate sensitivity of both methods to CO_2 and SST perturbations was comparable.

Climate simulations using mean sea surface temperature and CO_2 forcings representative of the early and late twentieth century were performed with the FVGCM. These showed that the global precipitation changed little with twentieth-century climate SST changes. However, the TPW increased with the increasing temperatures and so did the residence time of water vapor in the atmosphere. These simulations suggested that the global water cycling rate slowed for the simulation of twentieth-century climate. The processes that led to this conclusion have also been found in other GCM simulations (Roads et al. 1998; Douville et al. 2002). However, in these studies, the evolution of the water cycle or the statistical significance of the changes was not explored.

The evolution of the hydrologic cycle was tested using several 50-yr model simulations forced with observed time-varying SSTs. The SST warming in the 50-yr simulations drives increased evaporation and precipitation. Taken in isolation, this implies that the water cycle is intensifying. On the other hand, the total precipitable water increases with warming, and therefore the residence time of water increases, despite the increase of precipitation. The fact that water is spending more time in the atmosphere implies that the global cycling rate is decreasing. The 50-yr simulations from three models with different physical parameterizations all provide the same conclusions. The increasing trends of precipitation (and evaporation), TPW, and residence time were statistically significant in all the GCMs evaluated. It is important to stress that the results here are mostly all related to model simulations.

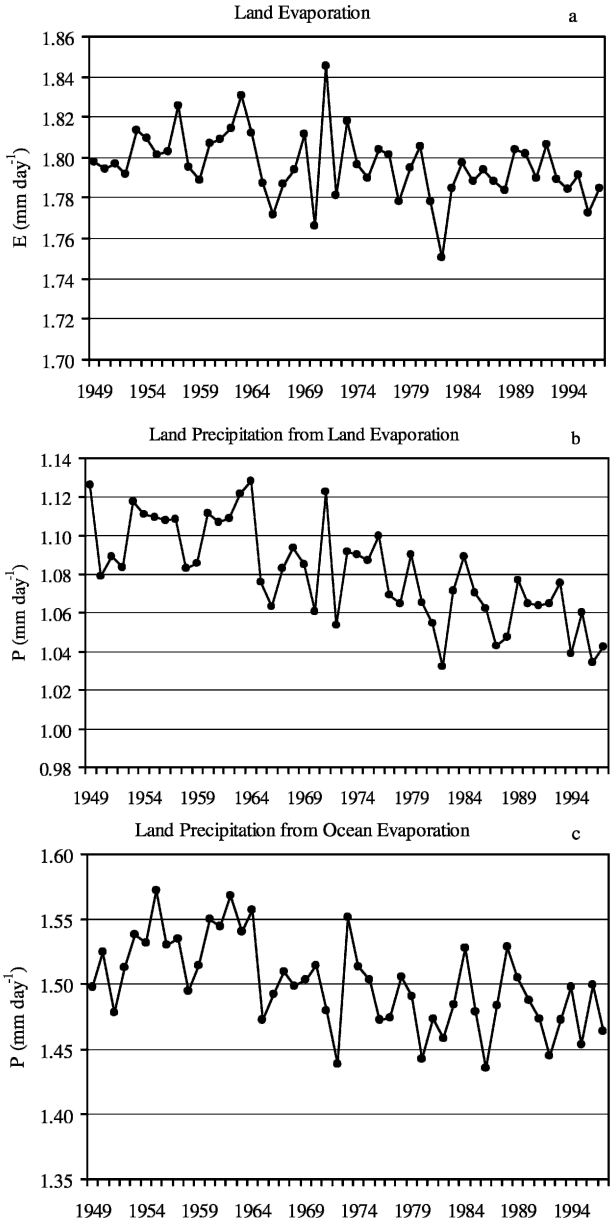

FIG. 13. Annual averages of land gridpoint (a) evaporation, (b) precipitation that occurs from land evaporation, and (c) precipitation that occurs from oceanic evaporation (not including the Antarctica continent in the spatial average).

TABLE 6. Trends as in Table 4, except for the land average time series of evaporation, precipitation that originated as land evaporation, and precipitation that originated as oceanic evaporation. The trends are computed for the 50-yr period and the last 25-yr period. Using the *t* statistic, all trend are significant (the trend is significantly different from 0) at the 1% level, except the italicized values, which are significant at 5%. Gray-shaded cells are not significant at 5%. The units are trend of precipitation in mm day^{-1} (50 yr)$^{-1}$.

Trend (50 yr)$^{-1}$	FVGCM land average 50 yr (mm day^{-1})	FVGCM land average 25 yr (mm day^{-1})
Evaporation	*−0.016*	0.006
P (land *E*)	−0.060	−0.062
P (ocean *E*)	−0.062	−0.020

Some regional correlations between the global residence time and SST were identified, including strong correlations to the tropical Pacific SST and to the Caribbean Sea. While the Amazon surface temperatures correlate to the global cycling rate, the corresponding surface evaporation did not. In the global average sense, the precipitation trend over land is decreasing (similar result as Kumar et al. 2004 for the Tropics), while the trend over oceans increases. The magnitude of these trends exceeds that of the total global average so that the increasing global trend is not necessarily representative of the globe. Furthermore, the contrasting land and ocean trends are not universally applicable to all regions. For example, the precipitation over the North American continent is increasing, while the precipitation trend over the Gulf of Mexico is decreasing.

Tracer diagnostics that delineate ocean and continental sources of water show that the continental sources of water for precipitation over land decrease continually throughout the last 50 yr of the twentieth century. The ocean sources of precipitation over land have virtually no trend over land in the last 25 yr of the twentieth century. There are distinct and significant changes in different directions depending on the region. Continental cycling of water appears to be decreasing in time, except for the central United States, where continental cycling may be increasing, as determined from numerical climate simulations. Further study is needed with a regional focus and with more detailed diagnostics that can quantify the local recycling rates. While global averages show statistically significant trends, temporal variability is increased for regions and continents. In addition, trends are difficult to identify in regional observations (Chase et al. 2003). The mean global trends identify the background state of the climate, and these must be observed with better quality for longer periods of time through satellite remote sensing.

Acknowledgments. We thank Dr. S.-J. Lin, Jiun-Dar Chern and Jon Radakovich for their support of the FVGCM in these studies. Michael Kistler and Philip Pegion provided support for the NSIPP C20C simulation, and James Kinter provided the COLA C20C GCM data online. Discussions with Drs. Alan Betts, Paul Dirmeyer, Robert Atlas, Yogesh Sud, and John Roads were particularly useful in evaluating these results. Three anonymous reviewers' comments greatly

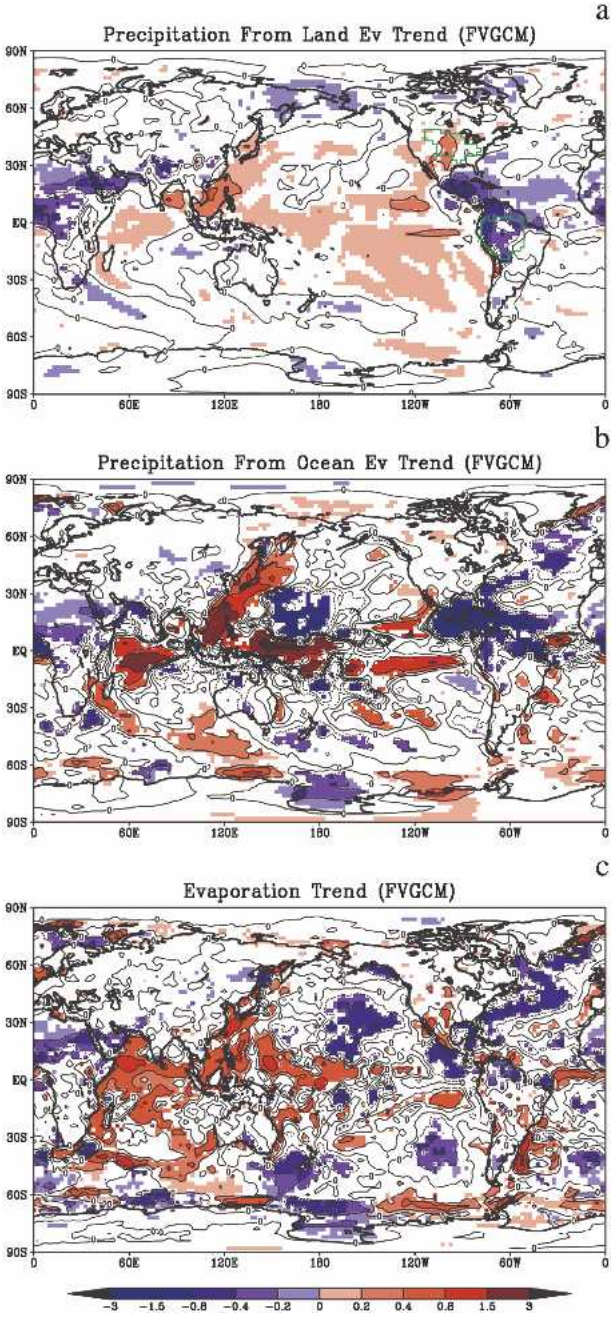

FIG. 14. Map of trends at model grid points for the FVGCM (a) precipitation that has a continental evaporative source, (b) precipitation that has an oceanic evaporative source, and (c) surface evaporation. The regions in (a) outlined in green denote the areas for Mississippi River and Amazon River basin averages.

improved the final version of this manuscript. This work was supported by the NOAA/NASA GAPP PACS Warm Season Precipitation Initiative and also by the NASA Global Water and Energy Cycle (GWEC) Program.

TABLE 7. Regional trends in the Mississippi River basin (MRB) and Amazon River basin (AMZ) of total precipitation (P), precipitation from land evaporation (P_l), precipitation from oceanic evaporation (P_o), evaporation within the region (E), and surface temperature (T_s). The units are mm day^{-1} and K (50 yr)$^{-1}$. Values are significant at 5%, except those that are italicized (10%) and shaded gray (not significant at 10%).

MRB	Trend (1949–98)	Trend (1974–98)
P	*0.16*	0.30
P_l	0.16	*0.23*
P_o	0.00	0.07
E	0.10	*0.18*
T_s	−0.10	0.77
AMZ		
P	−0.40	−0.84
P_l	−0.26	−0.43
P_o	*−0.14*	*−0.41*
E	0.01	*−0.15*
T_s	0.47	1.25

REFERENCES

Betts, A. K., J. H. Ball, M. G. Bosilovich, P. Viterbo, Y. Zhang, and W. B. Rossow, 2003: Intercomparison of water and energy budgets for five Mississippi sub-basins between ECMWF Reanalysis (ERA-40) and NASA-DAO fvGCM for 1990–1999. *J. Geophys. Res.,* **108,** 8618, doi:10.1029/2002JD003127.

Bonan, G. B., 1998: The land surface climatology of the NCAR land surface model coupled to the NCAR Community Climate Model. *J. Climate,* **11,** 1307–1326.

Bosilovich, M. G., 2002: On the vertical distribution of local and remote sources of water for precipitation. *Meteor. Atmos. Phys.,* **80,** 31–41.

——, and S. D. Schubert, 2001: Precipitation recycling in the GEOS-1 data assimilation system over the central United States. *J. Hydrometeor.,* **2,** 26–35.

——, and ——, 2002: Water vapor tracers as diagnostics of the regional hydrologic cycle. *J. Hydrometeor.,* **3,** 149–165.

——, Y. C. Sud, S. D. Schubert, and G. K. Walker, 2003: Numerical simulation of the North American monsoon water sources. *J. Geophys. Res.,* **108,** 8614, doi:10.1029/2002JD003095.

Briegleb, B. P., 1992: Delta-Eddington approximation for solar radiation in the NCAR Community Climate Model. *J. Geophys. Res.,* **97,** 7603–7612.

Brubaker, K. L., P. A. Dirmeyer, A. Sudradjat, B. S. Levy, and F. Bernal, 2001: A 36-year climatological description of the evaporative sources of warm-season precipitation in the Mississippi River basin. *J. Hydrometeor.,* **2,** 537–557.

Chahine, M. T., 1992: The hydrological cycle and its influence on climate. *Nature,* **356,** 373–380.

Chang, Y., S. D. Schubert, S.-J. Lin, S. Nebuda, and D.-W. Shen, 2001: The climate of the FVCCM-3 Model. NASA Tech. Memo. NASA/TM-2001-104606, Vol. 20, 127 pp.

Chase, T. N., J. A. Knaff, R. A. Pielke Sr., and E. Kalnay, 2003: Changes in global monsoon circulations since 1950. *Nat. Hazards,* **29,** 229–254.

Collins, W. D., and Coauthors, 2004: Description of the NCAR Community Atmosphere Model (CAM2). NCAR Tech. Note NCAR/TN-464+STR, 190 pp.

Dirmeyer, P. A., and F. J. Zeng, 1999: An update to the distribution and treatment of vegetation and soil properties in SSiB. COLA Tech. Rep. 78, 25 pp. [Available from the Center for

Ocean–Land–Atmosphere Studies, 4041 Powder Mill Road, Suite 302, Calverton, MD 20705.]

Douville, H., F. Chauvin, S. Planton, J.-F. Royer, D. Salas-Melia, and S. Tyteca, 2002: Sensitivity of the hydrological cycle to increasing amounts of greenhouse gases and aerosols. *Climate Dyn.,* **20,** 45–68.

Etheridge, D. M., L. P. Steele, R. L. Langenfelds, R. J. Francey, J.-M. Barnola, and V. I. Morgan, 1998: Historical CO_2 records from the Law Dome DE08, DE08-2, and DSS ice cores. *Trends: A Compendium of Data on Global Change*, Carbon Dioxide Information Analysis Center, Oak Ridge National Laboratory, U.S. Department of Energy. [Available online at http://cdiac.esd.ornl.gov/trends/co2/lawdome.html.]

Folland, C., J. Shukla, J. Kinter, and M. Rodwell, 2002: The Climate of the Twentieth Century Project. *CLIVAR Exchanges*, No. 7, International CLIVAR Project Office, Southampton, United Kingdom, 37–39.

Fu, R., R. E. Dickinson, M. Chen, and H. Wang, 2001: How do tropical sea surface temperatures influence the seasonal distribution of precipitation in the equatorial Amazon? *J. Climate,* **14,** 4003–4026.

Hack, J. J., 1994: Parameterization of moist convection in the National Center for Atmospheric Research Community Climate Model (CCM2). *J. Geophys. Res.,* **99,** 5551–5568.

Holtslag, A. A. M., and B. A. Boville, 1993: Local versus nonlocal boundary-layer diffusion in a global climate model. *J. Climate,* **6,** 1825–1842.

Houghton, J. T., Y. Ding, D. J. Griggs, M. Noguer, P. J. van der Linden, X. Dai, K. Maskell, and C. A. Johnson, Eds., 2001: *Climate Change 2001: The Scientific Basis*. Cambridge University Press, 881 pp.

Joussaume, S., R. Sadourny, and C. Vignal, 1986: Origin of precipitating water in a numerical simulation of July climate. *Ocean–Air Interact.,* **1,** 43–56.

Karl, T. R., and R. W. Knight, 1998: Secular trends of precipitation amount, frequency, and intensity in the United States. *Bull. Amer. Meteor. Soc.,* **79,** 231–241.

Kiehl, J. T., J. J. Hack, G. B. Bonan, B. A. Boville, D. L. Williamson, and P. J. Rasch, 1998: The National Center for Atmospheric Research Community Climate Model (CCM3). *J. Climate,* **11,** 1131–1149.

Kinter, J. L., III, D. DeWitt, P. A. Dirmeyer, M. J. Fennessy, B. P. Kirtman, L. Marx, E. K. Schneider, J. Shukla, and D. M. Straus, 1997: The COLA atmosphere–biosphere general circulation model. Volume 1: Formulation. COLA Tech. Rep. 51, 46 pp. [Available from the Center for Ocean–Land–Atmosphere Studies, 4041 Powder Mill Road, Suite 302, Calverton, MD 20705.]

Koster, R. D., and M. J. Suarez, 1992: A comparative analysis of two land surface heterogeneity representations. *J. Climate,* **5,** 1379–1390.

——, J. Jouzel, R. Suozzo, G. Russell, W. Broecker, D. Rind, and P. Eagleson, 1986: Global sources of local precipitation as determined by the NASA/GISS GCM. *Geophys. Res. Lett.,* **13,** 121–124.

Kumar, A., F. Yang, L. Goddard, and S. Schubert, 2004: Differing trends in the tropical surface temperatures and precipitation over land and oceans. *J. Climate,* **17,** 653–664.

Lin, S.-J., 2004: A "vertically Lagrangian" finite-volume dynamical core for global models. *Mon. Wea. Rev.,* **132,** 2293–2307.

——, and R. B. Rood, 1996: Multidimensional flux form semi-Lagrangian transport schemes. *Mon. Wea. Rev.,* **124,** 2046–2070.

——, and ——, 1997: An explicit flux-form semi-Lagrangian shallow-water model on the sphere. *Quart. J. Roy. Meteor. Soc.,* **123,** 2477–2498.

——, and ——, 1999: Development of the joint NASA/NCAR general circulation model. Preprints, *13th Conf. on Numerical Weather Prediction*, Denver, CO, Amer. Meteor. Soc., 156–160.

McFarlane, N. A., 1987: The effect of orographically excited wave drag on the general circulation of the lower stratosphere and troposphere. *J. Atmos. Sci.,* **44,** 1775–1800.

Milly, P. C. D., R. T. Wetherald, K. A. Dunne, and T. L. Delworth, 2002: Increasing risk of great floods in a changing climate. *Nature,* **415,** 514–517.

Moorthi, S., and M. J. Suarez, 1992: Relaxed Arakawa–Schubert: A parameterization of moist convection for general circulation models. *Mon. Wea. Rev.,* **120,** 978–1002.

Pegion, P. J., S. D. Schubert, and M. J. Suarez, 2000: An assessment of the predictability of northern winter seasonal means with the NSIPP 1 AGCM. NASA Tech. Memo. 104606, Vol. 18, Goddard Space Flight Center, Greenbelt, MD, 100 pp.

Ramanathan, V., and P. Downey, 1986: A nonisothermal emissivity and absorptivity formulation for water vapor. *J. Geophys. Res.,* **91,** 8649–8666.

Rayner, N. A., E. B. Horton, D. E. Parker, C. K. Folland, and R. B. Hackett, 1996: Version 2.2 of the global sea-ice and sea surface temperature data set, 1903–1994. Climate Research Tech. Note 74, Met Office, 21 pp.

——, D. E. Parker, E. B. Horton, C. K. Folland, L. V. Alexander, D. P. Rowell, E. C. Kent, and A. Kaplan, 2003: Global analyses of sea surface temperature, sea ice, and night marine air temperature since the late nineteenth century. *J. Geophys. Res.,* **108,** 4407, doi:10.1029/2002JD002670.

Roads, J. O., S. Marshall, R. Oglesby, and S.-C. Chen, 1996: Sensitivity of the CCM1 hydrological cycle to CO2. *J. Geophys. Res.,* **101,** 7321–7339.

——, S. C. Chen, S. Marshall, and R. Oglesby, 1998: Atmospheric moisture cycling rates. *GEWEX News*, Vol. 8, No. 3, International GEWEX Project Office, Silver Spring, MD, 1–10.

Schneider, E. K., 2002: The causes of differences between equatorial Pacific SST simulations of two coupled ocean–atmosphere general circulation models. *J. Climate,* **15,** 449–469.

Schubert, S. D., M. J. Suarez, P. J. Pegion, M. A. Kistler, and A. Kumar, 2002: Predictability of zonal means during boreal summer. *J. Climate,* **15,** 420–434.

——, ——, ——, R. D. Koster, and J. T. Bacmeister, 2004: Causes of long-term drought in the United States Great Plains. *J. Climate,* **17,** 485–503.

Straus, D., D. Paolino, J. Shukla, S. D. Schubert, M. J. Suarez, A. Kumar, and P. Pegion, 2003: Predictability of the seasonal mean atmospheric circulation during autumn, winter, and spring. *J. Climate,* **16,** 3629–3649.

Suarez, M. J., and L. L. Takacs, 1995: Documentation of the Aries-GEOS dynamical core: Version 2. NASA Tech. Memo. 104606, Vol. 5, 45 pp.

Trenberth, K. E., 1998: Atmospheric moisture residence times and cycling: Implications for rainfall rates and climate change. *Climatic Change,* **39,** 667–694.

Vose, R. S., R. L. Schmoyer, P. M. Steurer, T. C. Peterson, R. Heim, T. R. Karl, and J. K. Eischeid, 1992: The Global Historical Climatology Network: Long-term monthly temperature, precipitation, sea level pressure, and station pressure data. Environmental Sciences Division Publication 3912, ORNL/CDIAC-53, Carbon Dioxide Information Analysis Center, Oak Ridge National Laboratory, Oak Ridge, TN, 324 pp.

Watterson, I. G., 1998: An analysis of the global water cycle of present and doubled CO_2 climates simulated by the CSIRO

general circulation model. *J. Geophys. Res.,* **103** (D18), 23 113–23 129.
Wetherald, R. T., and S. Manabe, 1999: Detectability of summer dryness caused by greenhouse warming. *Climatic Change,* **43,** 495–511.
Xue, Y., P. J. Sellers, J. L. Kinter, and J. Shukla, 1991: A simplified Biosphere model for global climate studies. *J. Climate,* **4,** 345–364.
——, F. J. Zeng, and C. A. Schlosser, 1996: SSiB and its sensitivity to soil properties—A case study using HAPEX-Mobilhy data. *Global Planet. Change,* **13,** 183–194.
Yang, F., A. Kumar, M. E. Schlesinger, and W. Wang, 2003: Intensity of hydrological cycles in warmer climates. *J. Climate,* **16,** 2419–2423.
Zhang, G. J., and N. A. McFarlane, 1995: Sensitivity of climate simulation to the parameterization of cumulus convection in the Canadian Climate Centre general circulation model. *Atmos.–Ocean,* **33,** 407–446.